

Real-Time Partitioning of Octadecyl Rhodamine B into Bead-Supported Lipid Bilayer Membranes Revealing Quantitative Differences in Saturable Binding Sites in DOPC and 1:1:1 DOPC/SM/Cholesterol Membranes

Tione Buranda,* Yang Wu, Dominique Perez, Alexandre Chigaev, and Larry A. Sklar

Department of Pathology and Cancer Center, University of New Mexico School of Medicine, Albuquerque, New Mexico 87131

Received: July 14, 2009; Revised Manuscript Received: September 29, 2009

Quantitative analysis of the staining of cell membranes with the cationic amphiphile, octadecyl rhodamine B (R18), is confounded by probe aggregation and changes to the probes' absorption cross section and emission quantum yield. In this paper, flow cytometry, quantum-dot-based fluorescence calibration beads, and FRET were used to examine real-time transfer of R18 from water to two limiting models of the cellular plasma membrane, namely, a single-component disordered membrane, dioleoyl-L- α -phosphatidylcholine (DOPC), and a ternary mixture of DOPC, cholesterol, and sphingomyelin (DSC) membranes, reconstituted on spherical and monodisperse glass beads (lipobeads). The quenching of R18 was analyzed as the probe concentration was raised from 0 to 10 mol % in membranes. The data show a > 2 -fold enhancement in the quenching level of the probes that were reconstituted in DSC relative to DOPC membranes at the highest concentration of R18. We have parametrized the propagation of concentration-dependent quenching as a function of real-time binding of R18 to lipobeads. In this way, phenomenological kinetics of serum-albumin-mediated transfer of R18 from the aqueous phase to DOPC and DSC membranes could be evaluated under optimal conditions where the critical aggregation concentration (CAC) of the probe is defined as 14 nM. The mass action kinetics of association of R18 with DOPC and DSC lipobeads are shown to be similar. However, the saturable capacity for accepting exogenous probes is found to be 37% higher in DOPC relative to that for DSC membranes. The difference is comparable to the disparity in the average molecular areas of DOPC and DSC membranes. Finally, this analysis shows little difference in the spectral overlap integrals of the emission spectrum of a fluorescein derivative donor and the absorption spectrum of either monomeric or simulated spectrum of dimeric R18. This approach represents a first step toward a nanoscale probing of membrane heterogeneity in living cells by analyzing differential local FRET among sites of unique receptor expression in living cells.

Introduction

Octadecyl rhodamine B (R18) is a cationic amphiphile used in numerous studies including electronic energy transfer in organized molecular assemblies,^{1–4} membrane structure,^{5–13} and distances of closest approach between protein domains and membranes.^{14–20} In a series of papers,^{14–17} we have described the use of R18 as an acceptor in fluorescence resonance energy transfer (FRET) experiments, where we examined the dynamic structural transformation of a cell adhesion molecule, $\alpha_4\beta_1$ integrin in living cells. In these studies,¹⁷ the expression of $\alpha_4\beta_1$ integrins on the cell surface was presented in terms of a fluorescence measurement of an α_4 -specific peptide derivative 4-((*N'*-2-methylphenyl)ureido)phenylacetyl-L-leucyl-L-aspartyl-L-valyl-L-prolyl-L-alanyl-L-alanyl-L-lysine (LDV-FITC). Using the LDV-FITC probe as a donor, we developed a FRET assay where R18 partitions from the aqueous phase into cell membranes. The resultant FRET is analyzed in terms of a model that interprets acceptor surface density and transfer efficiency with respect to separation distances or distances of closest approach (r_{c1} in Figure 1)²¹ between the LDV-FITC probe and multiple R18 acceptors incorporated into the plasma membrane.

The plasma membrane is a system in which there is environmental heterogeneity. Lateral heterogeneity in mem-

branes is broadly defined in terms of the coexistence of ordered (saturated lipids and cholesterol) and disordered (unsaturated lipids) liquid phases of lipids.^{22–25} One essential element associated with heterogeneity among membrane lipids is the presence of submicroscopic transient domains around proteins and protein aggregates in signaling rafts.²² While there appears to be some consensus agreement regarding the existence of raft domains, questions still remain due to lack of direct visual evidence in living cells. When exogenous R18 is added to membranes, it is expected to distribute to varying extents among the environments in the plasma membrane. With this in mind, we have begun to study the coexistence of lipid domains in live cell membranes by using FRET to report, in real time, the differential distribution of R18 acceptors at the loci of two receptor sites in resting cells, as illustrated in Figure 1. The sites are defined by an $\alpha_4\beta_1$ integrin, previously proposed by us to be confined to liquid disordered domains,¹⁷ and the formyl peptide receptor (FPR) localized in liquid ordered domains in the plasma membranes of the same population of U937 cells (see Figure 1).²⁶

Progress in this work has been hindered by physiochemical characteristics of R18 that have produced confounding effects on our ability to analyze the transfer of R18 from the aqueous phase to local membrane sites. Issues of concern are as follows. (1) In the aqueous phase, amphiphilic R18 has an unknown critical aggregation concentration and exists in equilibrated

* To whom correspondence should be addressed. Phone: (505) 272 1259. E-mail: Buranda@unm.edu.

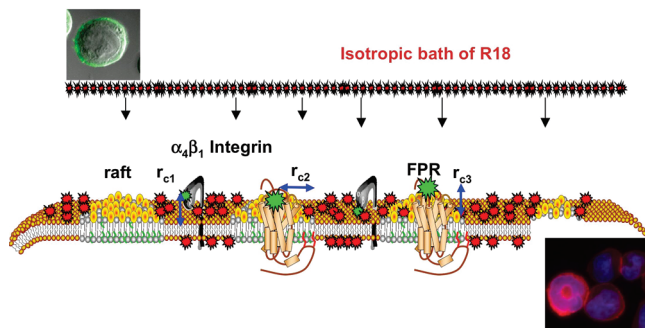


Figure 1. Model representation of the exposure of cells to an isotropic environment of R18 results in spatiotemporally heterogeneous staining of the cell membranes in a manner that reflects the heterogeneity of the plasma membrane. Sites of receptor expression are presented as fluorescently labeled ligands bound to $\alpha_4\beta_1$ integrin localized in liquid disordered domains and formyl peptide receptor (FPR) localized in membrane rafts. Lipid components of membrane rafts such as cholesterol and sphingomyelin are believed to confer membrane-condensing properties that make them less permeable to exogenous probes.^{31–33} The r_{ci} are the distances of closest approach between the FRET donor, FITC-labeled ligands, and R18 acceptors incorporated into the membrane. For the integrin, $r_{c1} = 25 \text{ \AA}$ is equivalent to the vertical separation between the integrin head group that bears LDV-FITC and the membrane.¹⁷ For the FPR, r_{ci} has vertical (height of the receptor binding site above the membrane, $r_{c2} = 0$) and lateral (width of the receptor and lipid raft that excludes R18 $r_{c3} = 13 \text{ \AA}$) components. The r_{ci} are based on the X-ray crystal structure of the GPCR rhodopsin II (PDB # 1h68). Micrographs show a cell bearing LDV-FITC before and after mixing with R18.

monomeric and aggregated forms^{8,27} even at nM concentrations. As for this problem, Vaz and co-workers^{28,29} have used a strategy by which amphiphile aggregation is circumvented by presenting the probe as a protein–(serum albumin) bound species. However, the mechanism (optimal reagent stoichiometry, kinetic and equilibrium constants) of this process has not been defined for R18. (2) R18 aggregates that are formed in water or in membranes have different spectroscopic properties than the monomers.³⁰ Therefore, if used as an acceptor in a FRET experiment, changes in the absorption cross section are likely to affect the degree of spectral overlap (J_{DA} term in eq 3) and thus the efficiency of FRET. It is therefore important to set quantitative limits on the membrane surface concentration of acceptors, where formation of dimers is deemed to be significant in order to establish appropriate constraints for accuracy in the analysis of FRET. On problem 2, several studies have described the propagation of concentration quenching of R18 in single-component and cholesterol-containing model membranes, including viral envelope membranes.^{5–13} It has been shown, that in general, cholesterol- and membrane-condensing lipids^{31,32} (i.e., lipids that confer a reduction of average molecular area per lipid in the bulk membrane)³³ affect a notable enhancement of self-quenching of R18 compared to that of unsaturated phospholipids.⁸

In anticipation of a rational use of R18 to stain live cell membranes, we have undertaken the present work to (a) define in a model system the conditions under which monomeric R18 can be delivered to membranes and (b) define the limiting surface density conditions for the onset of probe aggregation that causes significant changes to spectra and random distribution on the membrane surface.¹ Accordingly, in this paper, we have examined the transfer of R18 into two limiting models of the plasma membrane, namely, a single-component disordered membrane comprised of dioleoyl-L- α -phosphatidylcholine (DOPC) and a canonical raft model³⁴ ternary mixture of DOPC,

cholesterol, and sphingomyelin (DSC) lipids, reconstituted on spherical and monodisperse glass beads (lipobeads).³⁵ Quantitative flow cytometry measurements relying on a novel set of quantum-dot-based fluorescence calibration beads^{36,37} and FRET were used to quantify the surface labeling of model membranes with exogenous R18 probes. As a result, we define the phenomenological kinetics of serum-mediated transfer of monomeric R18 to lipobeads under optimal conditions, where the CAC is defined. The data also reveal that lipobeads accept a limited number of exogenous amphiphile probes and that DOPC membranes hold 37% more probes than DSC membranes, which is consistent with the relative average molecular areas of the model systems.³⁸ Subsequent studies will use the model framework developed here to analyze differential local FRET at sites of the receptor expression (Figure 1).

Experimental Section

A. Materials. 1,2-Dioleoyl-*sn*-glycero-3-phosphoethanolamine-*N*-(carboxyfluorescein) (fluorescein PE), 1,2-dioleoyl-*sn*-glycero-3-phosphoethanolamine-*N*-(lissamine rhodamine B sulfonyle) (rhodamine PE), and dioleoyl-L- α -phosphatidylcholine (DOPC), cholesterol, egg sphingomyelin (83.9% C16:0, 6.3% C18:0), and other minor longer chains (SM) were purchased from Avanti Polar Lipids, Inc. (Alabaster, AL). The 5 μm diameter glass beads were obtained in dry form from Duke Scientific Corp (Palo Alto, CA) and octadecyl rhodamine B chloride (R18) and 5-octadecanoylamino fluorescein (F18) were purchased from Molecular Probes (Eugene, OR) and used without further purification. Streptavidin-coated polystyrene particles (6.7 μm in diameter, 0.5% w/v) were purchased from Spherotech Inc. (Libertyville, IL). Streptavidin-coated quantum dots, QD585, were purchased from Invitrogen Corp (Carlsbad, CA). Phosphate-buffered saline (PBS) was purchased from Mediatech, Inc. (Herndon, VA). TRIS (10 or 25 mM Tris, 150 mM NaCl, pH 7.5) and HHB (30 mM HEPES, 110 mM NaCl, 10 mM KCl, 1 mM $\text{MgCl}_2 \cdot 6\text{H}_2\text{O}$, and 10 mM glucose, pH 7.4) buffer were used in the presence or absence of 0.1% human serum albumin (HSA). The human monoblastoid U937 cell line was purchased from ATCC (Rockville, MD).

B. Qdot-Labeled Microbeads. A detailed description of the preparation of fluorescence calibration beads can be found elsewhere.³⁶ Fluorescence calibration beads can be made for any fluorophore, under the rationale that the fluorescence intensity of any given molecule is proportional to $I_0\epsilon\phi$; I_0 is the intensity of the light source, ϵ is the absorption coefficient, and ϕ is the quantum yield of the fluorophore.

C. Determination of Probe Quantum Yields. Absorption and spectrofluorometric measurements were performed using a Hitachi model U-3270 spectrophotometer (San Jose, CA) and a Photon Technology International QuantaMaster Model QM-4/2005 spectrofluorometer (Lawrenceville, NJ), respectively. QD585, fluorescein, rhodamine B, R18, and F18 solutions were prepared in detergent micelle (1% Triton X-100) and vesicle suspensions. The optical densities at the absorption maxima of all solutions were kept at ≤ 0.02 , where the error due to inner filter effects is 2%.³⁹ Excitation and emission spectra were collected for all samples. Fluorescence intensity data were collected at each fluorophore's emission maxima using appropriate band-pass filters (Corion Corp., Holliston, MA; CVI Laser, Albuquerque, NM).

D. Supported Bilayer Membranes on Glass Beads. Lipid-coated glass beads (lipobeads) were prepared as previously described.³⁵ For the present study, lipobeads of various lipid compositions were prepared for the following applications: (a) to analyze the progression of self-quenching of R18 as a function

TABLE 1: Some Spectroscopic Characteristics of Molecular Probes

parameter	F18	QD585 (lot #45264A)	R18
$\epsilon(\text{M}^{-1} \text{cm}^{-1})@ \lambda_{\text{max}}^a$	80 000; ^b 72 600	—; 530 000	95 400; ^c 4750
$\epsilon(\text{M}^{-1} \text{cm}^{-1})@ \lambda_{\text{ex}}$			
quantum yield (ϕ_s) ^d	0.88 ^e	0.12 ^f	0.3 ^g
$\lambda_{\text{em max}}$ (nm) band-pass % T^h	520; 37	585; 65	585; 51
overlap integral $J_{\text{D-R18}}$ ($\text{cm}^3 \text{M}^{-1}$) ⁱ	3.35×10^{-13} ; 1.96×10^{-13} ; 2.8×10^{-13} ^j	—	3.75×10^{-13} ; 3.40×10^{-13} ; 3.09×10^{-13} ^k
R_0 -R18 (\AA) ^p	61.0; ^q 56.3; ^r 57.3 ^s		52.2; ^t 51.5 ± 1 ; ^u 51.3; ^v 48.0 ^w

^a Extinction coefficients obtained from www.probes.invitrogen.com unless stated otherwise; $\lambda_{\text{ex}} = 488$ nm for all experiments. ^b The extinction coefficients of fluorescein and derivatives vary from 85 000 for the NIST fluorescein solution standard reference material SRM 1932 to 75 000 for some FITC derivatives, and values are pH-dependent. We have selected a median number here, $\lambda_{\text{max}} = 598$ nm. ^c Taken from ref 59, $\lambda_{\text{max}} = 564$ nm. ^d Relative quantum yields, $\phi_s = \phi_{\text{ref}}(I_s/I_{\text{ref}})(\text{OD}_{\text{ref}}/\text{OD}_s)(n_s^2/n_{\text{ref}}^2)$, were calculated using the integrated intensity of the sample relative to fluorescein, $\phi_{\text{ref}} = 0.93$; or rhodamine B (0.31) in water (Magde et al., *Photochem. Photobiol.* **1999**). I_s and I_{ref} are the integrated band intensities. The optical densities (OD) of the sample (s) and reference (ref) were kept close. n is the index of refraction of the solvent, 1.32 for water. ^e Measured in 1% Triton X-100. ^f Measured in water, ϕ_s is accurate for the given lot number and excitation wavelength (see text and ref 37). ^g Measured in 1% Triton X-100. ^h Bandpass filters used in a standard model BD FACScan flow cytometer (cf. Figure 2 and Figure 4 in ref 37). ⁱ Calculated using eq 3. ^j Overlap with absorption spectrum of acceptor R18 in 1% Triton X-100. ^k Overlap with compound spectrum of monomers and aggregates of R18 water. ^l Resolved spectrum of R18 H-dimers (cf. Figure 2B). ^{m,n,o} Overlap integral for R18 emission and R18 absorption under conditions similar to those described in *j,k* and *l*, respectively. ^p R_0 values calculated using eq 2 for acceptor spectra measured in ^{q,t} 1% Triton X, ^{r,v} water, ^{s,w} water. ^u Taken from ref 2.

of its mole fraction (0–10 mol %) in a single-component DOPC lipid bilayer membrane and a 1:1:1 ternary mixture of DOPC/sphingomyelin/cholesterol (DSC) lipid membranes, (b) to analyze real-time FRET quenching of 0.025 mol % fluorescein PE doped in DOPC and DSC membranes, and (c) to analyze lateral separation of lipid phases in DSC bilayers doped with 0.25 mol % rhodamine PE.

Briefly, small unilamellar vesicles (SUVs) were prepared from 1 mM solutions of DOPC or 1:1:1 D/S/C in chloroform (210 μL total volume) in microfuge tubes. Fluorescent probes were added to the solution in the appropriate mole fraction as needed. The chloroform was removed by vacuum drying the samples using a CentriVap benchtop centrifugal vacuum concentrator (Labconco, Kansas City, MO) at room temperature for 1 h. After addition of 200 μL of Tris buffer (pH 7.5), the vesicle suspension was sonicated to optical clarity using a Branson sonifier (Branson Cleaning Equipment Co., Shelton CT). Acid- and peroxide-cleaned monodisperse glass beads³⁵ were then added to the SUV suspension with vortexing for 5 min. The lipobeads were then washed and resuspended in 1% HSA buffer a minimum of five times to remove excess vesicles. 1% HSA was added as a lipid-binding scavenger protein to facilitate the removal of vesicles (see Experimental Section subsection K for context). The final wash was performed in serum-free buffer. For long-term storage, beads were stored at 20 °C under argon or N_2 degassed conditions.

E. Fluorescence Quenching Measurements. Unless otherwise specified, bead suspensions were used at 1000 beads/ μL . The bead samples were transferred to cuvettes in 400 μL volumes with mini magnetic stir bars to maintain beads in suspension for fluorescence measurements using a Photon Technology International QuantaMaster Model QM-4/2005 spectrofluorometer (Lawrenceville, NJ), following standard protocols for such measurements.^{36,37} With the instrument set in kinetic mode, fluorescence intensities of the quenched R18-bearing lipobead suspensions were measured as a time course for 30 s, after which a 20 μL aliquot of 20% Triton X-100 was added to the bead suspension. In this way, the supported bilayer was completely solubilized, with the concomitant 100% de-quenching of R18. The increase in fluorescence intensity of the samples was corrected for dilution and then correlated to the degree of self-quenching of R18 at the various mole fractions in membranes. The results were plotted as a graph representing the relative quantum yield versus mole fraction of R18. This

graph (see Figure 3) was used to estimate the quantity of R18 associated with beads after a time course measurement. This analysis involved the centrifugation of and washing of beads after incubation with R18 for a desired time. The resuspended beads were then read at the spectrofluorometer before and after addition of Triton-X 100 as described above. The increase in fluorescence intensity was correlated to the mole fraction of R18 on the standard curve.

F. Measurement of the Transfer of R18 from the Aqueous Phase into Bead-Supported Membranes. Flow cytometric measurements were performed on a Becton–Dickinson FAC-Scan flow cytometer (Sunnyvale, CA) interfaced to a G4 Macintosh using the CellQuest software package. The FACScan was equipped with a 15 mW air-cooled argon ion laser. The laser wavelength was fixed at 488 nm. The time course of association between R18 and beads was typically measured by acquiring a 30 s baseline of donor fluorescence on beads or cells, then adding an aliquot of R18 to the sample, briefly vortexing (creating a 5–10 s gap in the time course), and resuming data collection continuously to some desired time (e.g., 150–300 s). Detailed protocols have been described elsewhere.^{14,17} The data output from a flow cytometer is normally expressed in terms of the mean fluorescence intensity of a population of cells or particles (mean channel fluorescence, MCF). Standard fluorescence calibration beads are used to convert the MCF value of cells to the number of fluorophore equivalents using eq 1

$$\frac{I_1}{I_2} = \frac{\epsilon_{\lambda_{\text{ex},1}}}{\epsilon_{\lambda_{\text{ex},2}}} \cdot \frac{\phi_1}{\phi_2} \cdot \frac{\%T_1}{\%T_2} \cdot \frac{\rho_1}{\rho_2} \quad (1)$$

where I_i are the measured intensities of the R18-bearing beads (1) and standard QD585 quantum-dot-bearing beads (2) irradiated by the same 488 nm, 15 mW laser; $\epsilon_{\lambda_{\text{ex},i}}$ are the molar extinction coefficients of R18 ($4750 \text{ M}^{-1} \text{cm}^{-1}$) and QD585 quantum dots ($530 000 \text{ M}^{-1} \text{cm}^{-1}$) at the excitation wavelength; and ϕ_i are the respective quantum yields of R18 and QD585 dots, lot # 452664A (see Table 1). It is important to note that the emission quantum yield of quantum dots varies from batch to batch;^{36,37} hence, the lot number of the streptavidin-functionalized dots used to tag our calibration beads is given here. The intrinsic quantum yield of R18 is 0.3,^{36,37} which decreases in proportion to the degree of self-quenching, as will be shown

in the Results section. The ρ_i are the site densities of R18 on the beads and quantum dots on the calibration beads, and % T is the percent fraction of fluorescence light transmitted through the band-pass filter and is used to account for the spectral mismatch between the R18 fluorophore and QD585 quantum dots. The values of these parameters are given in Table 1.

G. Calculation of R_0 . The characteristic distance at which the efficiency of energy transfer is 50% is defined as R_0 . R_0 is calculated (in Å units) using eq 2

$$R_0 = 9.79 \times 10^3 \text{ Å} (J_{\text{DA}} Q_{\text{D}} \kappa^2 n^{-4})^{1/6} \quad (2)$$

where, Q_{D} is the quantum yield of the donor in the absence of acceptors, κ^2 is the geometric factor that depends on the relative orientation of the donor and acceptor transition dipoles (κ^2 is usually assumed to be 2/3, a value which corresponds to the randomization of donor–acceptor orientations by their rotation or diffusion), n is the refractive index (1.33) of the medium between the donor and acceptor moieties, and J_{DA} is the overlap integral that expresses the degree of overlap between the donor emission and acceptor absorption

$$J_{\text{DA}} = \int_0^\infty F_{\text{D}}(\lambda) \epsilon_{\text{A}}(\lambda) \lambda^4 d\lambda / \int_0^\infty F_{\text{D}}(\lambda) d\lambda \quad (3)$$

$F_{\text{D}}(\lambda)$ is dimensionless intensity, representing a corrected emission spectrum of the donor normalized to unity at the band maximum, $\epsilon(\lambda)$ is an extinction coefficient expressed in units of $\text{M}^{-1} \text{ cm}^{-1}$, and λ is wavelength that is expressed in units of cm; thus, the overall units of J are $\text{M}^{-1} \text{ cm}^3$. Calculated values of R_0 for probes used herein are given in Table 1.

H. Random Energy Transfer to Multiple Acceptors in Two Dimensions. Energy-transfer data were analyzed using the formalism developed by Wolber and Hudson,²¹ which involves the steady-state intensity of randomly distributed donor molecules quenched by acceptor molecules on an infinite plane. This is given by the expression in eq 4a

$$\frac{Q_{\text{DA}}}{Q_{\text{D}}} = \int_0^\infty e^{-\lambda} e^{-\Gamma(2/3)\pi R_0^2 c \lambda^{1/3}} d\lambda \quad (4a)$$

$$\frac{Q_{\text{DA}}}{Q_{\text{D}}} = 0.6463e^{-4.7497R_0^2 c} + 0.3537e^{-2.0618R_0^2 c} \quad (4b)$$

Q_{DA} and Q_{D} are the respective quantum yields of the donor in the presence and absence of acceptors, $\lambda = t/\tau$ is the ratio of time t and the intrinsic lifetime τ of donor molecules, $\Gamma(2/3)$ is the standard mathematical gamma function, and c is the two-dimensional concentration of acceptors per unit area, expressed in terms of R_0^2 or $C = R_0^2 c$. Equation 4 is applicable for values of C the range from 0 to 0.5.²¹ Equation 4b represents an approximate solution to the numerical integration of eq 4a, where the coefficients corresponds to an exact solution for the series approximation for the value of the distance of closest approach, $r_c = 0$, between randomly distributed donors and acceptors on an infinite plane. The $r_c = 0$ is applicable to DOPC membranes, where the donor and acceptor probes are both randomly distributed in a homogeneous membrane without the presence of a boundary lipid (membrane raft), which excludes or hinders the partitioning of R18 such as with DSC membranes (cf. Figure 3).

I. Incorporation of R18 into and Dissociation from Bead-Supported DOPC Membranes. To measure the dissociation of R18 from beads, a relatively low concentration of 0.44 μM R18 was added to a suspension of 2×10^6 beads in 0.1% HSA HHB buffer and allowed to incubate at 37 °C for 1 min. The sample was then centrifuged, and the beads were resuspended in 1 mL HHB buffer containing 1% HSA. Once again, a high concentration of HSA was used here to capture the desorbing R18 probes, thus minimizing probe rebinding. To analyze the dissociation kinetics of R18 from resuspended beads, the fluorescence intensity of the beads was measured using a flow cytometer at regular intervals over a period of over 30 h, and the beads were kept at 37 °C and in suspension by stirring in a temperature-controlled sample holder.

J. Confocal Microscopy Imaging. Beads were placed in a sample chamber (Model PDMI-2 Open Perfusion Microincubator). Confocal microscope imaging was performed on a Zeiss 510 LSM inverted microscope at 20 °C, as previously described.³⁵

K. Kinetic Analysis of the Association of R18 and Beads. Most amphiphiles (phospholipids and their derivatives, long-chain fatty acids, etc.) are predisposed to aggregate in aqueous solution when used at concentrations that are higher than their critical aggregation or micelle concentration (CAC or CMC).^{28,29} Serum albumin is the principal physiological carrier of highly insoluble long-chain fatty acids ($\geq \text{C}_{14}$) in the circulation.^{40–43} Consumption for energy metabolism requires the rapid transport of fatty acids between serum and cells. Consequently, the characteristic time of approach to the binding equilibrium must be extremely fast and is typified by a rapid on-rate and a relatively rapid dissociation rate to facilitate the delivery of the fatty acids to their metabolic sites.^{42,44–46} Accordingly, serum albumin has been used in membrane staining buffers to reduce the concentration of free amphiphile to some desired level below the CMC.^{28,29} The free monomeric amphiphile that transfers from the aqueous phase to the membrane is continuously replenished with amphiphiles that dissociate from the protein-bound state.^{28,29} This process is represented in a mass-action-based kinetic model, as shown in eq 5



The kinetic interaction of serum albumins with amphiphile probes or various fatty acids is well studied, and as such, we have relied upon the conceptual framework established by Vaz and co-workers^{28,29,47} for our kinetic analysis. To that purpose, for eq 5a, an intrinsically fast binding rate constant ($k_1 \geq 10^6 \text{ M}^{-1} \text{ s}^{-1}$) and dissociation rate constant ($0.1 \leq k_{-1} \leq 0.9 \text{ s}^{-1}$)⁴² is expected (vide supra). These interactions are largely driven by hydrophobic interactions such that a limiting range of values can be estimated based on chain lengths.^{43,48} For the practical purpose of maintaining a monomeric concentration of free R18, the relative concentrations of serum albumin and R18 must be $([\text{HSA}]_0 \gg [\text{R18}]_0)$, such that [HSA] remains unchanged throughout the course of the experiments. Each HSA molecule is assumed to bear six receptor sites for long-chain ($>\text{C}_{14}$) fatty acids/amphiphiles.^{40,42,43} Our analysis makes the simplifying assumption that the kinetic differences among the intraprotein binding sites cannot be resolved by our experimental method,

in line with single-exponential dissociation characteristics of fatty acids from serum albumin.⁴²

In eq 5b, lipids represents “free-volume” units or holes of dimensions approximately equal to or greater than the cross-sectional area of the R18 probes that represent binding sites in the lipid bilayer membrane.^{49,50} The definition of a binding site in lipid membranes is complicated, and often, the formalism that is used depends on the experimental situation.⁵¹ The most common model treatment of the partitioning of a probe into lipid membranes is one that is expressed in terms of a ratio of membrane-associated probes and probes in the aqueous phase, that is, $[R18]_{\text{membrane}}/[R18]_{\text{aq}}$. This model contains no explicit information on binding sites and is, in principle, most applicable when the probe concentration is much smaller than the quantity of membrane lipids.⁵¹ Several approaches, which include the concept of binding sites, have been discussed in a book by Gennis.⁵¹ Our experimental situation is mitigated by the use of monodisperse-sized beads, which present a defined supporting platform for a finite quantity of membrane lipids. Quantitative assessment of probe binding to measurable and finite binding sites on beads allows us to treat our data using a homogeneous kinetic model based on mass action. In view of that, the association of R18 with beads was then analyzed using a set of coupled ordinary differential rate equations derived from eq 5.

$$r_1 = k_1[R18][HSA] - k_{-1}[R18 \cdot HSA] \quad (6a)$$

$$r_2 = k_2[R18][\text{lipids}] - k_{-2}[R18 \cdot \text{lipids}] \quad (6b)$$

Results

A. Spectroscopic Properties of R18 Relative to Quantum Dot Fluorescence Calibration Beads. Figure 2A shows a graph of superimposed absorption (left axis) and emission spectra (right axis) of R18 and 585 nm quantum dots. The emission spectra are scaled such that the peak value represents the maximum quantum yield values of R18 and QD585, respectively. Spectroscopic data are summarized in Table 1.

Numerous studies have shown that xanthene dyes, such as rhodamine B, tend to form aggregates in the aqueous phase.^{30,52–56} These aggregates exist as either nonfluorescent “H-dimers” or fluorescent “J-dimers” depending on the geometry adopted by the monomer constituents.⁵⁷ H-dimers are formed when two monomer transition moments are in coplanar geometry, whereas J-dimers are at oblique angles.^{53,57} H-dimers of rhodamine B are formed in polar solvents such as water, whereas J-dimers dominate in nonpolar environments such as ethanol.³⁰ Elucidation of the spectral characteristics of R18 under our experimental conditions is important to establish the modes of self-quenching.

The absorption spectra of 1×10^{-6} M R18 in 1% Triton X-100 and regular buffer are shown in Figure 2B. The emission spectra of F18 and R18 are also presented for the purpose of displaying spectral overlap with the absorption spectra (vide infra). The absorption cross section and emission properties of monomeric R18, solubilized in vesicles or Triton X-100, are close to those of the parent molecule, rhodamine B.⁵⁸ Some differences can be found in the absorption maxima and extinction coefficients of the rhodamine B ($\lambda_{\text{max}} = 554$ nm; $\epsilon = 120\,000 \text{ M}^{-1} \text{ cm}^{-1}$)³⁰ and R18 ($\lambda_{\text{max}} = 565$ nm; $\epsilon = 95\,400 \text{ M}^{-1} \text{ cm}^{-1}$).⁵⁹ In 1% Triton X-100, R18 aggregates are solubilized, to the extent that they exist in monomeric form. In water, the absorption spectrum of R18 aggregates is characterized by a significant loss in the oscillator strength of the lowest-energy band (0–0 transition)⁶⁰ centered at 570 nm. Others^{30,54} have

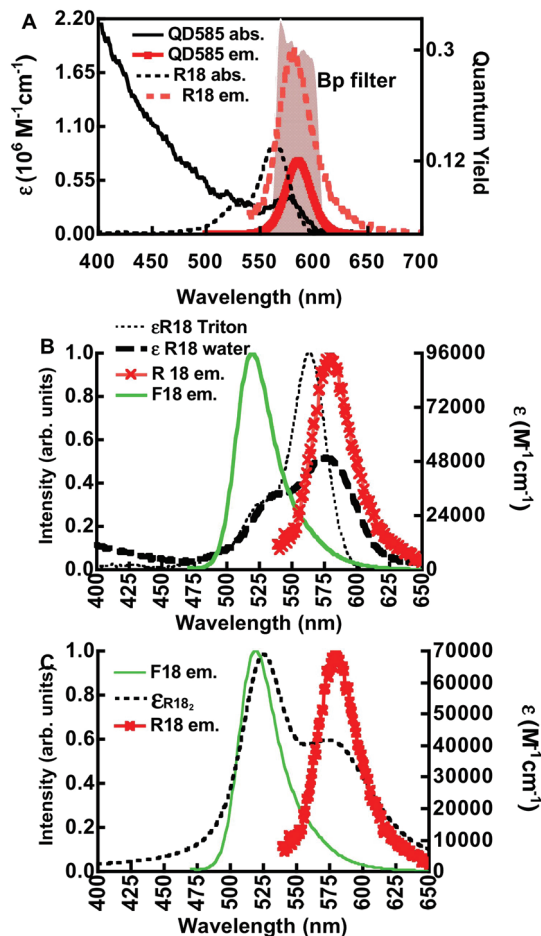


Figure 2. (A) Fluorescence calibration and spectroscopic properties of R18 and QD585 dots. (Right-hand ordinate) Plot of absorption spectra of R18 (R18 abs.) and QD585 quantum dots (QD585 abs.). (Left ordinate) Plot of quantum distribution functions of emission of R18 (R18 em.) and QD585 (QD585 em.) normalized by the maximum quantum yield of each probe. The shaded spectral region represents a band-pass filter centered at 580 nm and a component of one of three detection channels of a BD flow cytometer. (B) (Left ordinate) Plot of normalized emission spectra of F18 (F18 em.) and R18 (R18 em.). (Right ordinate) Plot of absorption spectra of R18 solubilized in Triton X-100 ($\epsilon R18$ Triton) and neat buffer ($\epsilon R18$ water). (C) (Left ordinate) Plot of normalized emission spectra of F18 (F18 em.) and R18 (R18 em.). (Right ordinate) Resolved spectrum of the R18 H-dimer ($\epsilon R18_2$) modeled from the compound spectrum of R18 aggregates ($\epsilon R18$ water) in (B) using parameters (λ_{max} , ϵ , and bandwidth fwhm) taken from Selwyn and Steinfeld (see text for details).³⁰

shown that rhodamine B forms ground-state complexes with an average association constant (K_a) of $\sim 10^4$ M. On the basis of the putative K_d , one would expect only a small fraction of the dye to be dimerized at 1 μM . Nevertheless, for R18, the C18 long acyl chain on R18 is expected to confer surfactant-like properties, such that aggregation occurs at much lower concentrations.⁶¹ Selwyn and Steinfeld³⁰ have examined the absorbance of rhodamine B over the concentration range of 10^{-7} to 10^{-3} M. From these measurements, they resolved the absorption spectra of H- and J-aggregates. Spectral parameters (e.g., λ_{max} , bandwidth (fwhm), ϵ), of the absorbance spectrum of a H-dimer from Selwyn and Steinfeld³⁰ were used to resolve the absorption spectrum of H-dimers in our compound spectrum of monomers and aggregates using Igor Pro Software package (Lake Oswego, OR). The absorption spectrum of $R18_2$ consists mainly of two overlapping bands with peak wavelengths fixed

at 524 and 574 nm. The bandwidths were estimated to be 50 and 90 nm, respectively. The extinction coefficients at the two peaks, which were given by Selwyn and Steinfeld³⁰ relative to rhodamine B monomers ($1.2 \times 10^5 \text{ M}^{-1} \text{ cm}^{-1}$), were then scaled relative to the extinction coefficient of R18 of $9.54 \times 10^4 \text{ M}^{-1} \text{ cm}^{-1}$ at 564 nm.⁵⁹ The simulated absorption spectrum of a R18₂ H-dimer is shown in Figure 2C.

B. Calculation of R_0 . The overlap integrals (J_{DA} in eq 3) for F18 and R18 donor emission and R18 and (R18)₂ acceptor absorption spectra were calculated, and the results are summarized in Table 1. The outcome shows very little distinction in the relative magnitudes of J_{DA} for monomeric or dimeric forms of R18. Because of the inverse sixth power dependence (eq 2) of dipole–dipole interactions, changes in the relative size of parameters such as κ^2 and J_{DA} have little effect on the magnitude of R_0 . Thus, a 64-fold change in J_{DA} is necessary to effect a 2-fold change in the numerical value of R_0 if all other parameters in eq 2 are held constant. The magnitude of κ^2 normally spans the $0 \leq \kappa^2 \leq 4$ range. The values of 0 and 4 correspond to the cases where the donor and acceptor dipole moments are orthogonal and comprise a mixture of parallel and antiparallel moments, respectively.⁶² Two common values of κ^2 in membranes are 0.667, corresponding to the randomization of donor–acceptor orientation by rotational diffusion of donors and acceptors before FRET, and 0.476, the static randomization of donor–acceptor orientations that otherwise remain constant during the lifetime of the donor.^{62,63} The value for static randomization normally applies to 3D measurements, whereas 0.405 has been suggested as the more appropriate value for 2D membrane surface measurements.⁶⁴ The most commonly used approximate value of 0.667 yields a maximum error of 35%. These limiting values of κ^2 produce a variation in the value of R_0 of $\sim 5\%$. The usual error encountered in most experiments is no more than 10%.⁶² The applicability of 0.667 to our data is later demonstrated in Figure 8.

C. R18 in Bead-Supported Bilayer Membranes. Bead-supported bilayer membranes were formed by vesicle fusion on hydrophilic glass surfaces as previously described.^{35,65} Depending on composition and temperature, the typical membrane was separated from the substrate by a thin (10–30 Å) layer of water and, like natural membranes, possessed macroscopic long-range fluidity with mobile components of both leaflets freely diffusing over the entire surface of the support.^{35,66–68} Figure 3 shows confocal fluorescence micrographs of DOPC and DSC bilayer membranes supported on 5 μm glass beads. DOPC (C18:1–C18:1) has two unsaturated acyl chains, with a low chain melting temperature (-20°C). SM (C16:0) has saturated chains that melt at $\sim 41^\circ\text{C}$.⁶⁹ The (1:1:1) ternary mixture of DOPC, SM, and cholesterol has two coexisting phases, namely, liquid-ordered (L_o) SM and cholesterol-enriched and liquid-disordered (L_d) DOPC and cholesterol depleted phases, below the miscibility transition temperature of $T_m = 35\text{--}40^\circ\text{C}$.⁶⁹ At 20°C , phase-separated L_o and L_d domains are recorded by the acyl-chain-unsaturated fluorescent probe 18:1 rhodamine PE that is excluded from SM-rich L_o and colocalizes with the DOPC-rich L_d domain.²⁴

D. Self-Quenching of R18 Enhanced in DSC Membranes Relative to That in DOPC Membranes. Figure 3A shows a plot of the relative quantum yield of bead-borne R18 as a function of its % mole fraction ($\% \chi$) in the DOPC and DSC bilayer membranes. A comparison of our DOPC data to vesicle data (e.g., see Figure 5 from Johansson and Niemi⁵⁸) shows that the onset and degree of self-quenching of R18 over a 0–10 $\% \chi$ range is enhanced by a factor of 2 on beads compared to

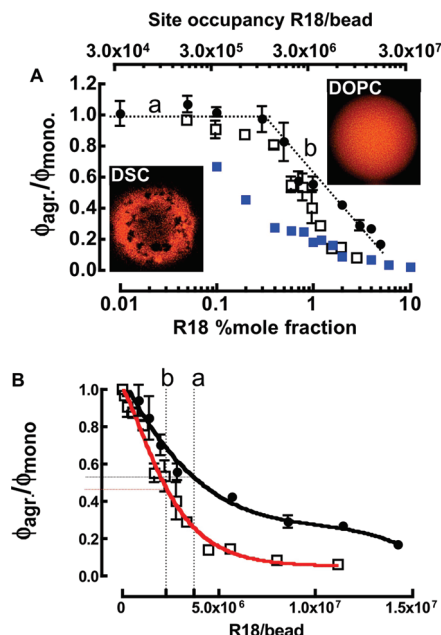


Figure 3. (A) Confocal micrographs of DOPC (top) and DSC beads (bottom) at 20°C . Relative quantum yield $\phi_{\text{agr}}/\phi_{\text{mono}}$ of R18 solubilized in supported lipid membrane bilayers: (filled circles) DOPC at 37°C , (open squares) DSC at 37°C , and (filled squares) DSC at 20°C on beads. ϕ_{mono} refers to the quantum yield of soluble rhodamine B or R18 in Triton X-100. (a) The dotted line marks the site occupancy/mol fraction region below the onset of self-quenching. (b) The line shows the site occupancy/mol fraction region in which the self-quenching of R18 in DOPC membranes changes linearly on the log scale. (B) Relative quantum yield $\phi_{\text{bead}}/\phi_{\text{mono}}$ of R18 on DOPC (filled circles) and DSC (open squares) lipobeads as a function of site coverage at 37°C . The curves represent theoretical fits to the data using eqs 7 and 8, respectively. The vertical dotted lines refer to the maximum site occupancy numbers of R18 at the end of a binding time course (in Figure 5) for (a) DOPC and (b) DSC beads. Horizontal tie lines to the y-axis represent the degree of self-quenching in R18-occupied DOPC and DSC lipobeads.

that on vesicles. It turns out that on beads, R18 is effectively localized in the outer leaflet of the membrane and poorly randomized in both leaflets, as is the case in vesicles. This was confirmed by a potassium iodide collisional-quenching experiment,⁶⁰ where the addition of 100 mM KI quenched nearly all fluorescence. The efficient quenching was taken to be consistent with the localization of the R18 head group at the membrane/water interface in the outer leaflet where it was exposed to collisional encounter with KI. The localization of R18 in the outer leaflet is likely to be imposed by the unfavorable steric interaction of the chromophore with the bead surface as the water layer does not provide sufficient separation between bulk membranes and the substrate surface.⁶⁸ Self-quenching in DOPC membranes is constant between room temperature and 37°C , whereas in DSC membranes, partial exclusion of R18 from the gel-like L_o phase at temperatures below the $35\text{--}41^\circ\text{C}$ miscibility transition temperature⁶⁹ yields a significant increase in quenching because of the increase in the surface concentration of R18 in the L_d domains.

Cholesterol- or membrane-condensing lipids (with relatively small molecular area footprints)^{33,38} significantly enhance quenching due to relatively higher surface concentration of probes in the condensed membranes.⁸ Figure 3B shows a plot of the relative quantum yield of R18 versus the numbers of R18 on beads at 37°C . For later convenience, it is useful to represent the propagation of self-quenching (SQ) as a function of site

occupancy on a bead by some empirical formalism that best fits the data points. The DOPC data were fit to a third-order polynomial (eq 7), while the DSC data were fit to a double exponential function (eq 8)

$$SQ_{R18/DOPC} = 1.0 - 1.56 \times 10^{-7} R18/\text{bead} + 7.4 \times 10^{-15} (R18/\text{bead})^2 - 9.95 \times 10^{-23} (R18/\text{bead})^3 \quad (7)$$

$$SQ_{R18/DSC} = 0.0168 \exp^{-5.59 \times 10^{-9} R18/\text{bead}} + 0.99 \exp^{-3.86 \times 10^{-7} R18/\text{bead}} + 0.014 \quad (8)$$

For use in a kinetic model, it is practical to represent eqs 7 and 8 in terms of a molar concentration at 1×10^9 beads/L as used in our experiments.

$$SQ_{[R18 \cdot DOPC]} = 1.01 - 1.28 \times 10^8 [R18 \cdot DOPC] + 6.9 \times 10^{15} [R18 \cdot DOPC]^2 - 1.37 \times 10^{23} [R18 \cdot DOPC]^3 \quad (9)$$

$$SQ_{[R18 \cdot DSC]} = 0.01 \exp^{-2.4 \times 10^8 [R18 \cdot DSC]} + 0.99 \exp^{-2.3 \times 10^8 [R18 \cdot DSC]} + 0.014 \quad (10)$$

E. Quantification of Bound R18 Using Fluorescence Calibration Beads. Flow cytometry is a multiparameter measurement tool that enables the simultaneous analysis of light scatter and several colors.⁷⁰ The measurements are based on the analysis of quenching of the emission of the donor probe excited with the 488 nm line of an argon ion laser. There is sufficient off-resonance absorbance ($\epsilon = 4750 \text{ M}^{-1} \text{ cm}^{-1}$; cf. Table 1) of the blue tail of the R18 acceptor at 488 nm. It is important to note that the magnitude of fluorescence intensity from direct excitation is experimentally demonstrated to be orders of magnitude larger than what one would expect from sensitized emission. Accordingly, the partitioning of R18 into membranes was concurrently measured as the emission output of direct excitation of R18 at 488 nm as well as energy-transfer quenching of donor fluorescence. The data are shown in Figure 4. To the casual observer, the association of R18 with DOPC and DSC lipobeads appears to be governed by similar kinetics where the number of saturable “binding sites” on DOPC beads turns out to be higher than that on DSC. Turning to the FRET data, it is unfortunate that full donor quenching is realized at a relatively low surface concentration of R18, which constitutes a small fraction of the time course. The quantitation of R18 on beads by calibration beads will be presented first, while some quantitative aspects of the FRET assay will be examined later.

Equation 1 (see Table 1 for parameter values) was used to convert the raw mean channel fluorescence data to effective numbers of R18 probes/bead. At this time, the quantum yield of monomeric R18 was applied throughout the time course, without correcting for the self-quenching, which is known to propagate with increasing surface concentration (cf. Figure 3). The data were plotted as shown in Figure 4. The effective occupancies/bead were then converted to effective molar concentration units on 1×10^9 beads/L. Equation 11 was used to analyze the kinetics of association of R18 with lipobeads.

$$\frac{d[R18 \cdot \text{lipids}]}{dt} = r_2 SQ_{[i]} \quad (11)$$

where, $SQ_{[i]}$ is represented by eqs 9 and 10 for DOPC and DSC, respectively.

Finally, eq 11 and all of the rate equations for the variable parameters of the kinetic scheme shown in eq 5a were solved numerically using the Runge–Kutta method for values of reaction rate constants k_i and k_{-i} using Berkeley Madonna Software (Berkeley, CA) or Scientist Software (Micromath, St. Louis, MO).

The dissociation rate constant, k_{-2} , of R18 from lipobeads was determined by measuring the desorption of low surface concentration R18 (that is, below the self-quenching regime) from beads over a 30 h period and analyzing the loss of fluorescence intensity of washed lipobeads (not shown). The $t_{1/2}$ for the desorption of R18 from beads was ~ 17 h or $k_{-2} = 1.2 \times 10^{-5} \text{ s}^{-1}$. In context, it is worth noting that shorter single-chain amphiphiles ($\leq C_{14}$ chain) are very labile⁷¹ and readily desorb from membranes ($t_{1/2} \approx 0.02 \text{ s}$),⁷² while double-chain amphiphiles of the same length are slow ($t_{1/2} \sim 10^{-5} \text{ s}$).⁷³ The well-documented strong interaction between R18 and membranes^{12,74} is attributable in part to the length of its C18 acyl chain and head group.^{12,75} The surface concentration of R18 at the end of the time course (that is, $t = 200 \text{ s}$) was estimated by correlating the degree of dequenching of the beads (after detergent solubilization) to R18/bead from the readout of our standard curves in Figure 3.

Under our experimental conditions, it was not possible to experimentally measure the other three unknown rate parameters. Constraints were placed on the values of k_1 and k_{-1} based

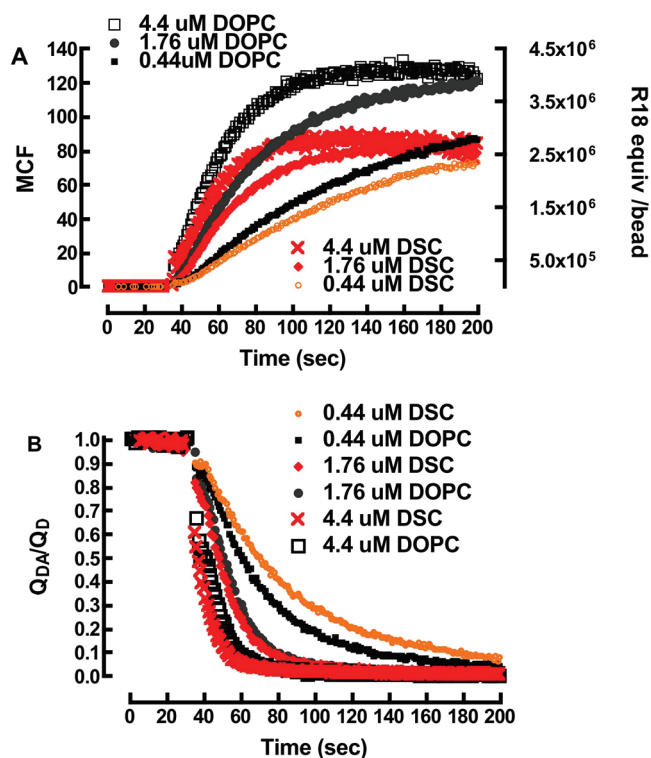


Figure 4. Partitioning of R18 into membranes. (A) Direct excitation of R18. (Left y-axis) Plot of the mean channel fluorescence (MCF) versus time and readings for partitioning of R18 into DOPC and DSC membranes. (Right y-axis) Nominal site occupancy of R18 equivalents on self-quenched beads derived from fluorescence calibration beads. (B) FRET time course of FRET quenching of F18 after addition of R18.

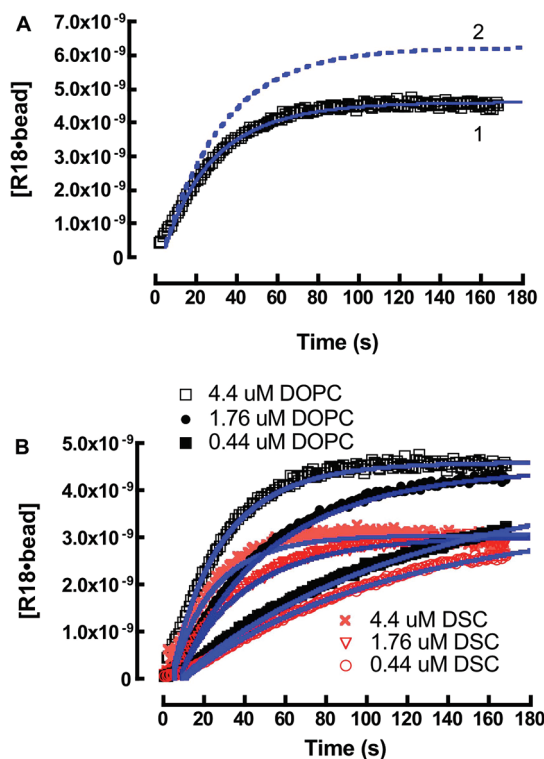


Figure 5. (A) Kinetic analysis of real-time association of R18 with DOPC beads. A theoretical fit of the data set was derived from the following rate constants: $k_1 = 1.0 \times 10^6 \text{ M}^{-1} \text{ s}^{-1}$, $k_{-1} = 0.73 \text{ s}^{-1}$, $k_2 = 1.2 \times 10^6 \text{ M}^{-1} \text{ s}^{-1}$, and $k_{-2} = 1.2 \times 10^{-5} \text{ s}^{-1}$. (1) The theoretical fit (eq 11) of experimental data describing the association and self-quenching of $4.4 \mu\text{M}$ R18 with DOPC beads. (2) Simulation of the propagation of unquenched [R18] on DOPC beads. (B) Kinetic analysis and simulation of the association of 0.44, 1.76, and $4.4 \mu\text{M}$ R18 and 400 000 lipobeads bearing DOPC and DSC membranes in $400 \mu\text{L}$ of buffer containing 0.1% HSA.

on literature values for long-chain fatty acids ($\text{C}_{16-18:0}$) (k_1 : 1×10^6 – $10^7 \text{ M}^{-1} \text{ s}^{-1}$ and k_{-1} : 0.1 – 0.9 s^{-1});^{42,76} only k_2 was unconstrained. Thus, the rate parameters k_1 , k_{-1} , and k_2 are nominally defined to within an order of magnitude. In this way, a theoretical fit of the $[\text{R18}]_0 = 4.4 \mu\text{M}$ data set yielded the following nominal rate constants: $k_1 = 1.0 \times 10^7 \text{ M}^{-1} \text{ s}^{-1}$, $k_{-1} = 0.73 \text{ s}^{-1}$, $k_2 = 1.2 \times 10^6 \text{ M}^{-1} \text{ s}^{-1}$, and experimentally measured $k_{-2} = 1.2 \times 10^{-5} \text{ s}^{-1}$. The rate constants used here represent an upper limit to the constraints placed on k_1 . The analysis is summarized in Figure 5A. Curve 1 shows an overlay of the quenched experimental data with a theoretical fit to eq 11. Curve 2 represents the evolution of (unquenched) $[\text{R18} \cdot \text{lipids}]$ derived from the theoretical fit when the self-quenching term $\text{SQ}_{[i]}$ in eq 11 is fixed to unity. The derived rate parameters were then fixed and used to simulate the $[\text{R18}]_0 = 0.44$ and $1.76 \mu\text{M}$ DOPC data sets. The DSC data sets were analyzed using the same rate constants. As shown in Figure 5B, the simulated curves are reasonably correlated to the experimental data. The correlation between the early kinetic data, $<10 \text{ s}$, and theoretical fits was generally poor because of the dead time and laminar flow recovery time of the flow cytometer.⁷⁷ At this time, it is important to note that a different combination of rate parameters, which fall within an order of magnitude of the ones given here, can fit the data just as well. To limit the number of unknown variables, we considered applying quasi-stationary or steady-state kinetics.⁷⁸ To demonstrate conditions for the applicability of quasi-steady-state treatment, it is useful to show the distribution of $[\text{R18}]_0 = 4.4 \mu\text{M}$ among $97.0 \mu\text{M}$ HSA, free R18 monomers, and DOPC

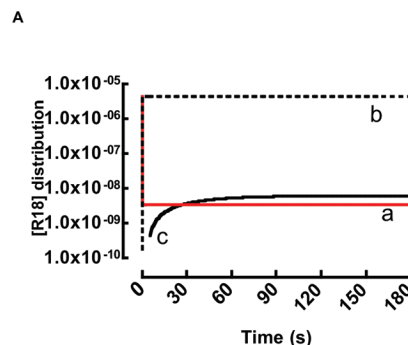


Figure 6. Real-time distribution kinetics of $4.4 \mu\text{M}$ R18 among (a) aqueous phase, (b) HSA, and (c) DOPC beads derived from eq 5a using the high estimates of rate parameters, $k_1 = 1.0 \times 10^7 \text{ M}^{-1} \text{ s}^{-1}$, $k_{-1} = 0.73 \text{ s}^{-1}$, $k_2 = 1.2 \times 10^6 \text{ M}^{-1} \text{ s}^{-1}$, and $k_{-2} = 1.2 \times 10^{-5} \text{ s}^{-1}$. Here, the addition of a $2 \mu\text{L}$ aliquot of $4.4 \mu\text{M}$ DMSO-solubilized R18 to 0.1% HSA buffer yields all but $\sim 3 \text{ nM}$ (curve a) of HSA·R18 complexes (curve b) in $\ll 0.1 \text{ s}$, during which time equilibrium is established (eq 5a). At equilibrium, the residual ($\sim 3 \text{ nM}$) R18 binds to the beads (curve c). The steady-state concentration of free R18 is replenished by fresh monomers dissociating from (b) to maintain equilibrium. It is later shown using a more accurate set of rate parameters that residual $[\text{R18}]_{\text{eq}}$ is $\sim 10 \text{ nM}$ (see Results subsection F text for details).

membranes over the experimental time course using the nominal rate parameters from the kinetic model so far. As shown in Figure 6, the rate parameters for eq 5a allow for an a priori prediction of a subsecond characteristic time for equilibration (that is, $t_{\text{eq}} = 5t_{1/2} = 3.5/(k_1[\text{R18}]_0 + k_{-1})$)⁷⁹ (see (a) in Figure 6). The 2.5 nM range working concentration of the free probe, $[\text{R18}]_{\text{eq}}$, is maintained at a constant value throughout the time course, (that is, when $[\text{R18}]_0 \gg [\text{lipids}]$) as the probe that is consumed by the beads is replenished by the dissociation of monomeric R18 from HSA·R18 complexes (cf. eq 5a).^{28,29}

Under these conditions, a quasi-steady-state model⁷⁸ can be used to derive a single rate parameter, such as an effective rate constant (k_{eff} in eq 12 and derived in Appendix A) to describe the association of monomeric R18 and lipobeads. The k_{eff} is constant for the data set because the variability of the individual parameters is self-correcting within the confines of parameter space that yields a good fit to the experimental data.

$$\frac{d[\text{R18} \cdot \text{lipids}]}{dt} = k_{\text{eff}}[\text{lipids}][\text{R18} \cdot \text{HSA}] \text{SQ}_{[i]} \quad (12a)$$

$$k_{\text{eff}} = \frac{k_{-1}k_2}{k_1[\text{HSA}]} \quad (12b)$$

It can be shown that a simultaneous fit of experimental data to eqs 11 and 12 yields the same result. Thus, it is instructive to evaluate k_{eff} over a range of k_i parameter space defined by fixing one of the given k_i 's while varying the other two rate parameters. Adjustment to $[\text{HSA}]_0$ leads to a predictable change in k_{eff} , for example, a 10-fold increase in $[\text{HSA}]$ affects a 10-fold decrease in k_{eff} (data not shown). The model analysis also yielded the following site occupancies at the end of each time course for DOPC and DSC, respectively: ($0.44 \mu\text{M}$) 2.4×10^6 and 1.56×10^6 ; ($1.76 \mu\text{M}$) 3.5×10^6 and 2.15×10^6 ; and ($4.4 \mu\text{M}$) 3.7×10^6 and 2.34×10^6 . To summarize Figure 5 data, a singular $k_{\text{eff}} \approx 1 \times 10^4 \text{ M}^{-1} \text{ s}^{-1}$ represents a robust overall rate at which R18 partitions into DOPC and DSC membranes, where

the significant finding of these experiments is the 37% difference in the absolute numbers of saturable binding sites associated with DOPC and DSC membranes. As shown in Figure 3, the maximum site occupancies fall in a range where the differences in the self-quenching of R18 in DOPC and DSC membranes are minimal and within experimental error. Thus, the observed quantitative differences in R18-occupied DOPC and DSC lipobeads are less susceptible to confounding effects that are likely at higher mol % (see Discussion).

F. Estimates of the Critical Aggregation Concentration of R18. In water, the 18 carbon chain of R18 confers surfactant-like properties to the probe. It has been shown that surfactants whose aliphatic chains are longer than 12 carbons are likely to form aggregates at concentrations that are much lower than their CAC.⁶¹ To the best of our knowledge, the CAC of R18 in water is thus far unknown. The difficulty in its determination can be attributed to its tendency to form self-quenching dimers² at very low concentrations.²⁷ As previously discussed with respect to eq 5, a large stoichiometric excess of HSA was used to ensure that the equilibrium concentration of free amphiphile was kept below its heretofore unknown CAC. The good correlation between experiment and theory suggests that under our experimental conditions, the equilibrium concentration of monomeric R18 was maintained below the CAC. It has been over 30 years since Aniansson, Wall, and co-workers⁸⁰ developed a theoretical formalism for describing the aggregation of amphiphiles, in terms of a stepwise process as given in eq 13, in our nomenclature. Where $R18_1$ denotes monomeric R18, and $R18_a$ denotes an aggregate of a R18 molecules, $k_{\pm a}$ represent the respective association and dissociation rate constants. The k_a may vary according to the coefficient due to cooperativity effects.⁸¹



If k_2 (in eq 5) $\gg k_a$, then one might expect subtle differences between theory and experiment, whereas if $k_2 \leq k_a$, then the applicability of eq 6 is expected to fall off very sharply. To establish some baseline expectations about the perturbative effects of aggregation on the applicability of the eq 6, we excluded serum albumin from some measurements. The results shown in Figure 7A for the 0.25 μM R18 suggest that $k_a > k_2$. The fluorescence intensity of the serum-free sample is significantly lower than that of the 0.1% HSA-containing sample. This suggests that amphiphile aggregates transfer poorly, if at all, to membranes.

We then examined the transfer kinetics of R18 to lipobeads suspended in 0.1% HSA buffer over a concentration range of 0.25 to 17.6 μM . As demonstrated above, the correlation between model simulations and experiments was reasonable up to 4.4 μM R18. When $[R18]_0$ was raised to 6.6 μM , the differences between theoretical expectations and experiment became significant, as shown in Figure 7B. The early binding rate is slower than expected, and the probe intensity turns over and decreases without reaching a plateau. The behavior is similar to the positive control experiment shown in Figure 7A. At 17.6 μM R18, increased aggregation produces a complex kinetic trace. The decrease in intensity is likely due to the association of beads with highly self quenched aggregates or due to detergent-like solubilization of membranes by R18 micelle aggregates.⁸²

The inferred onset of aggregation at $[R18]_0 = 6.6 \mu\text{M}$ implies that the equilibrium concentration of free R18 at this level is

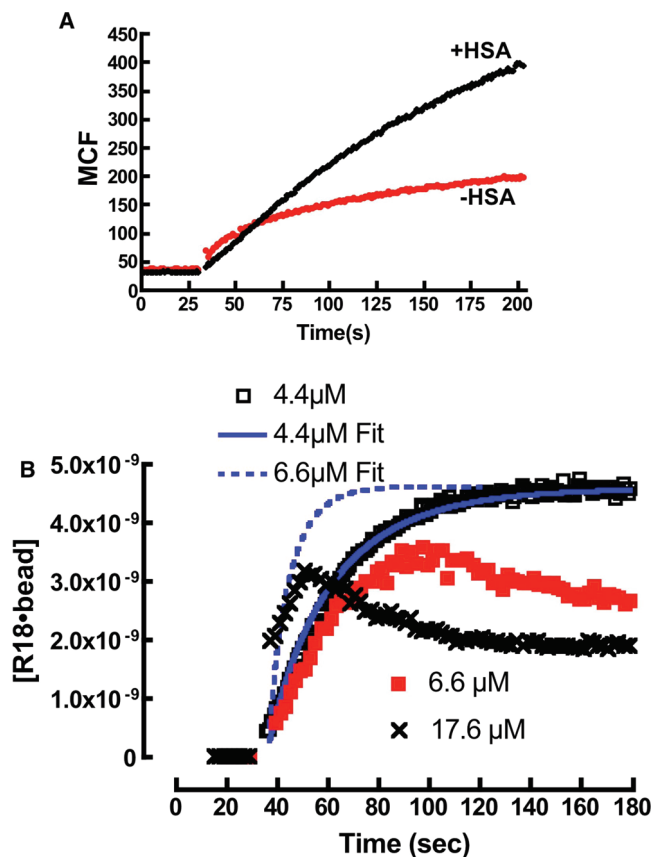


Figure 7. (A) Plot of R18 binding to DOPC membranes in buffer containing 0.1% HSA and no HSA. In the absence of HSA, the intensity of R18 is much lower than that of HSA-containing media. (B) Probe aggregation leads to anomalous binding kinetics of R18 to beads. At 4.4 μM , the equilibrium concentration of R18, $[R18]_{eq}$ is below the CAC, and the binding curve shows agreement with a model (4.4 μM Fit) that ignores the effects of aggregation (eq 13). At 6.6 μM , the binding time course for the binding of R18 to beads is shown to deviate from model predictions (6.6 μM Fit). This is attributed to probe aggregation when the equilibrium concentration of free R18 exceeds CAC. The anomalous binding characteristics increase at 17.6 μM .

equal or greater than the CAC. $[R18]_{eq}$ was evaluated from the equilibrium constant, $K_a = (k_1)/(k_{-1})$ (see Figure 6). As discussed in subsection E of the Results, the uncertainties in the derived rate parameters are within a factor of 10. Figure 8A shows a plot of $[R18]_{eq}$ versus $[R18]_0$ for each concentration of R18 used herein. The lower and upper limiting values of K_a represent the range of uncertainty in $[R18]_{eq}$. The initial estimate of CAC was assumed to fall within the range of values of $[R18]_{eq}$ for $[R18]_0 = 6.6 \mu\text{M}$, that is, 3–42 nM. The CAC was subsequently resolved in an assay designed to measure the onset of aggregation.⁸³ The intensity of R18 solubilized in Triton X-100 was measured using a spectrofluorometer and compared to the intensity of the same concentration of R18 dissolved in water over a 1–100 nM concentration range. In Triton X-100, the intensity of R18 increased linearly with concentration, whereas in water, the intensity of R18 emission was not proportional to concentration due to probe aggregation. Below 10 nM, the relative intensities of R18 in water and Triton X-100 were comparable or within a factor of 2. The differences at low concentration were attributed to dimerization of R18 in water.²⁷ Figure 8B shows a plot of the intensity ratio of 1% Triton X-100 and water-solubilized R18 versus the logarithm of $[R18]_0$. With increasing concentration, an acute change in the slope of the ratiometric intensity measurements is shown to have an inflection point at 14 nM. The inflection point was determined to be

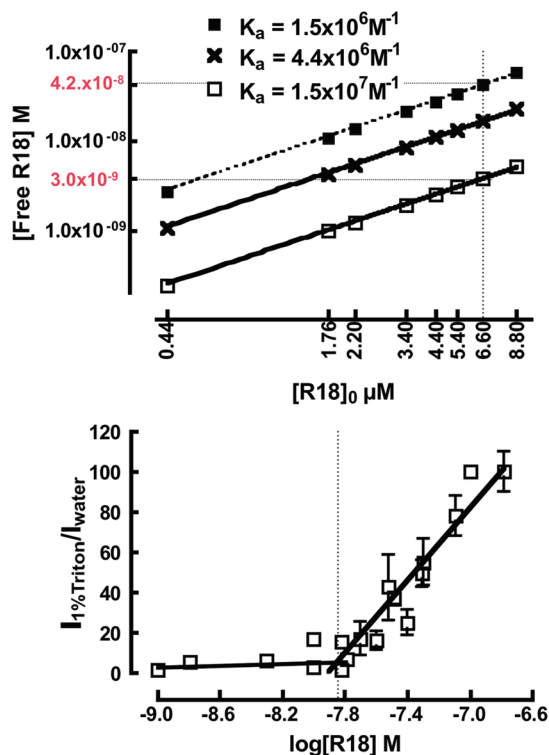


Figure 8. (A) Plot of free $[R18]_{eq}$ versus $[R18]_0$. Values of $[R18]_{eq}$ were calculated using three values of K_a derived from theoretical fits of experimental data (see Figure 5). Top and bottom curves represent the upper and lower limits of K_a based on the uncertainty in the rate parameters. The middle curve represents the K_a value based on the CAC determination (see text for details). The vertical dotted line marks the concentration of bulk R18 at which probe aggregation was inferred. The limiting values of $[R18]_{eq}$ are identified along the lower and upper curves by dotted lines that intersect the y-axis at 3 and 42 nM, as shown. (B) Determination of CAC from a plot of the ratiometric assay of the fluorescence intensity of R18 solubilized in 1% Triton X-100 and water versus $\log[R18]$. The inflection point is equal to the CAC value of ~ 14 nM.

the CAC. It is worth noting that the experimental determination of CAC enables an improvement in the accuracy of the derived rate parameters as one imagines that the experimental value of CAC is much closer to the correct value of $[R18]_{eq}$ than a factor 10. In this way, the rate parameters rescaled to CAC are $k_1 = 3.2 \times 10^6 \text{ M}^{-1} \text{ s}^{-1}$, $k_{-1} = 0.73 \text{ s}^{-1}$, and $k_2 = 3.6 \times 10^6 \text{ M}^{-1} \text{ s}^{-1}$. The values of $[R18]_{eq}$ derived from the CAC-corrected rate parameters are shown as the middle line in Figure 8A.

G. FRET Assay for Quantitation of Bound R18 Acceptors on Beads. The RET data (y-axis, Q_{DA}/Q_D in Figure 4B) were converted to an assay of C , the number of acceptors per R_0^2 on beads (see eq 4a), and plotted as shown in Figure 9A. The Forster-based formalism of RET²¹ is accurate within a narrow range of acceptor densities of 0–0.5 acceptors/ R_0^2 . The approach assumes random and uniform distribution of molecules over the defined $4\pi r^2$ surface area of the $5 \mu\text{m}$ beads. This assumption is accurate in DOPC membranes at the limiting acceptor density of 0.5 acceptors/ R_0^2 . Because of the phase-segregated domains in DSC membranes, the degree of random and uniform distribution of acceptors over the total surface area of the bead is uncertain. Accordingly, only the results of the FRET quantification assay on DOPC beads are appropriate for comparison to fluorescence calibration beads. The data in Figure 9A were converted to an absolute number of R18 acceptors on each bead by multiplying the derived values of C by 2.1×10^6 , the total number of R_0^2 -sized ($R_0 = 61 \text{ \AA}$) unit areas on a

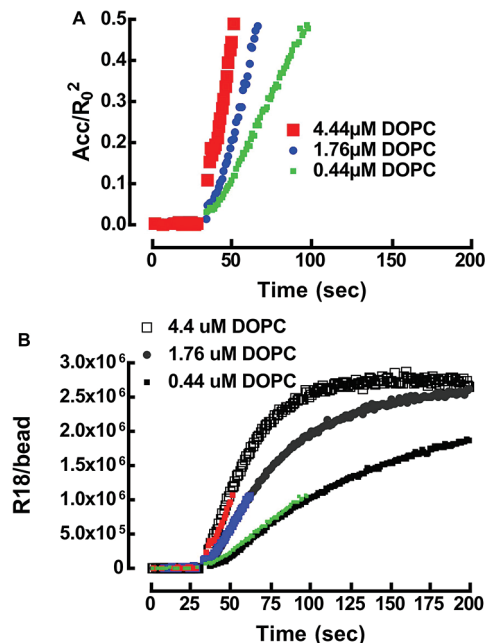


Figure 9. (A) Analysis of FRET in DOPC beads. Plot of the R18 surface concentration in terms of acceptors/ R_0^2 versus time for three concentrations of R18 as listed in the legend. (B) Correlation of FRET-derived values of absolute R18 acceptors on DOPC beads and the R18/bead derived from calibration beads for three titers of $[R18]_0$ shown in the legend.

$5 \mu\text{m}$ bead. The converted data were superimposed over the fluorescence calibration bead-derived data from Figure 5, as shown in Figure 9B. It is also worth noting that the onset of significant probe aggregation (see Figure 3) on beads occurs at site occupancies that are much greater than the upper limit for accuracy of the Wolber and Hudson²¹ approach, 0.5 acceptors/ R_0^2 ($\sim 1 \times 10^6$ R18/bead). Therefore, the data are not confounded by self-quenching in this regime. We took the close agreement between the two data sets as validation of the FRET scheme as we have previously authenticated the applicability of these beads in comparison to commercial standards.³⁶ The accuracy of FRET depends on the derived value of R_0 , where probe aggregation is expected to effect perturbations in J_{DA} and κ^2 (cf. Results subsection B). Our analysis of the spectral overlap between the donor F18 and dimeric R18 has shown that the change in J_{DA} is minimal (Table 1). The close correlation between the calibration bead and FRET data suggests that the assumed value of $\kappa^2 = 2/3$ is valid for this system. This is consistent with the argument presented by Fayer and co-workers² that a Poisson distribution and random orientation are accurate to describe R18 acceptors in micelles as long as the mole fraction is less than 0.1 (or 10 mol %).

Discussion

This study establishes a quantitative approach for examining membrane structure and lateral heterogeneity attributed to coexisting lipid domains in live cell membranes. The assay is based upon the differential dynamics of partitioning of an exogenous fluorescent lipid probe into supported lipid bilayer membranes of different composition. We examined the association kinetics of R18 with lipid bilayers presented as the liquid-disordered, L_d , phase prepared from DOPC and the liquid-ordered, L_o , phase prepared from a ternary mixture of DOPC, SM, and cholesterol (DSC), where DSC membranes are modeled after canonical lipid rafts.⁸⁴

In lipid bilayer membranes, free volume or area refers to the overall, randomly distributed void space not occupied by lipids and water in the membrane.^{85,86} Lateral diffusion of lipids in membranes has been analyzed in terms of “free-area” models that assume that diffusive mobility is facilitated by random density fluctuations, where the redistribution of free area creates voids greater than some critical area next to a diffusing molecule, which then fills the void by lateral translation.^{50,85,86} In this way, the rate of lateral diffusion has been shown to decrease as a function of cholesterol content or other membrane-condensing acyl-chain-saturated lipids such as SM⁸⁷ due in part to a decrease in free area.⁸⁸ Free-volume or -area properties are important to the permeation of amphiphiles and in our application provide a direct measure of free space that is accessible to penetrant molecules.⁵⁰ Accordingly, the partitioning of R18 into lipid membranes is regulated by the frequency of the density fluctuations that open up voids that are equal to or greater than the cross-sectional area of the probe.⁵⁰

With its two unsaturated acyl chains, DOPC occupies a relatively large molecular area (71 \AA^2), whereas saturated chains of SM occupy less volume (62 \AA^2).³⁸ The “condensing effect” of cholesterol is driven by the mutual orientation of cholesterol’s planar sterol ring and the hydrophobic tail, which enables hydrogen-bonding interactions with saturated acyl chains of SM.^{32,33} Previous studies have shown that a membrane mixture equivalent to the 1:1:1 DSC mixture herein is expected to present a molecular area per lipid of $40\text{--}47 \text{ \AA}^2$.³⁸ DSC is accordingly expected to present less free-volume capacity for exogenous probes.⁵⁰

We have relied on the substantial body of literature of the photophysical properties of rhodamine B^{2,30,54,58} to establish a quantitative assay that directly measures free-volume properties of lipid membranes. In a polar environment, aggregation brings the rhodamine xanthene rings into mutual proximity as coplanar nonfluorescing “H-dimers”⁵⁷ that are characterized by a blue shift in their absorption spectrum (Figure 2C) relative to the monomer.⁵⁷ Titration of R18 in membranes of different composition has yielded differential levels of self-quenching that are sensitive to molecular area.⁸ While the process by which concentration-dependent self-quenching propagates in membranes has been attributed to energy transfer^{2,3,8,58} or molecular interactions,⁸⁹ it has been difficult to establish a clear basis for it. We have therefore taken a phenomenological approach to developing an analytical method of describing the proliferation of self-quenching of R18 as a function of its mole fraction in membranes supported on monodisperse-sized beads (see eqs 7 and 8). In earlier studies, others^{8,12,58} have shown that the onset of probe aggregation that is manifested by self-quenching of R18 solubilized in single-component vesicle membranes was linear over the 1–9 mol % fraction range^{12,58} but exhibited exponential characteristics⁸ in cholesterol-containing membranes. On DOPC lipobeads, we show that the onset of quenching occurs at $\chi \geq 0.3 \text{ mol \%}$ and linearly increases on the logarithmic scale up to $\chi \approx 5 \text{ mol \%}$. On DSC lipobeads, the onset of quenching (at 37°C) occurs at $\chi \leq 0.1 \text{ mol \%}$. These data are best represented in terms of a fit to an n th order polynomial and exponential function, respectively. Equations 7 and 8 allow for the parametric treatment of surface-concentration-dependent quenching as a function time, which enables the real-time kinetic analysis of the association of R18 and lipobeads.

Elsewhere, Vaz and co-workers have recently used stopped flow measurements to examine the kinetics and thermodynamics of association of a two-acyl chain probe, NBD-dimyristoylphos-

phatidylethanolamine (NBD-DMPE)⁸³ and a single acyl chain NBD-lysomyristoylphosphatidylethanolamine (NBD-lysoMPE)⁷² with large unilamellar vesicles in L_d (POPC) and L_o (1:1 POPC/Chol and 6:4 SM/Chol) phases. These studies have shown that the association kinetics of two-footed NBD-DMPE with all membranes is 4 orders of magnitude slower than those measured for NBD-lysoMPE, where the forward rate constants were close to the diffusion limit. The authors then concluded that the difference in the forward binding rates of the amphiphiles to L_d and L_o phases was due to differential random density fluctuations, which mediate the presentation of holes of large enough size to accommodate surface-associated amphiphiles.⁷² In analogous fashion, our assay allows us to evaluate the free-area differences in DSC and DOPC membranes on the basis of their saturable capacity to hold exogenous R18 (Figures 4–6). The 37% fewer sites in DSC membranes are well-correlated to the expected drop in molecular area due to the condensing effects of cholesterol and SM, as previously discussed.^{33,38}

When the mol % fraction of “endogenous” R18 is extended to 10 mol % in bulk membranes, DSC membranes display a >2 fold enhancement of quenching (Figure 3) relative to that of DOPC at 37°C . This measurement represents an interesting way in which the structural differences between DSC and DOPC are amplified over 500 fold. When the probe is reconstituted as an endogenous part of the model membrane, its homotypic interactions are regulated by its equilibrium distribution in the bulk membrane in which it is an integral part (Figure 3). It is reasonable to expect that as its mol % fraction increases, the probe and the membrane will redistribute to an equilibrium. Accordingly, it has been shown that probes such as *N*-(lissamine rhodamine B sulfonyl)dipamitoylphosphatidylcholine form aggregates in membranes above some threshold in a manner which depends on the membrane composition, temperature, and pH.^{8,89} Elsewhere, it has also been argued that the surface distribution and orientations of membrane probes are no longer randomized at mol % fractions exceeding 10 in DOPC-like membranes or Triton X-100 micelles.² The introduction of exogenous probes to preassembled membrane structures is governed by the equilibrium distribution of free volume.^{50,72,86} It is therefore gratifying that in our real-time experiments, the exogenous R18 probes that are accepted into the pure DOPC and DOPC bulk membranes are limited to surface occupancies that are up to $\sim 3 \text{ mol \%}$ of the bulk membrane. At this concentration, the perturbation of the membrane structures of DOPC and DSC by “endogenous” R18 impurities (Figure 3) is minimized, in such a way that the calibration concentration quenching curves (eqs 7 and 8) are more likely to accurately represent the quenching conditions of real-time kinetics. We consider the good correlation between the differential free-volume capacity of the two model membranes and their molecular area differences to be a good indicator of the applicability of our parametric kinetic model.

One of our goals in undertaking this study was to establish a quantitative and intuitive framework in which to estimate the surface density of probes on membranes using a known set of thermodynamic and kinetic parameters. The equilibrium distribution of $[\text{R18}]_0$ among three phases is given in eq 14, where $[\text{R18}]_{\text{eq}}$ is the free probe in the aqueous phase, $[\text{R18}]_{\text{lb}}$ is the surface concentration on lipobeads in units of mol/dm^2 , $A_{\text{lb}} = (n4\pi r^2/V_w)$ is the ratio of the membrane surface area supported by $n = 1 \times 10^9$ beads to the 1 dm^3 volume of water (V_w) used in our experiment, and $[\text{HSA} \cdot \text{R18}]_{\text{eq}}$ is the serum-bound protein.

$$[R18]_0 = [R18]_{eq} + [HSA \cdot R18]_{eq} + [R18]_{lb}A_{lb} \quad (14)$$

The formal relationship between eq 14 and model kinetic and equilibrium parameters is described in Appendix A. From Figure 6, we estimate that the distribution of $[R18]_0 = 4.4 \mu\text{M}$ among the aqueous phase, serum albumin, and beads is according to the following proportions: $[R18]_{eq} \approx 10.0 \text{ nM}$, $[HSA \cdot R18]_{eq} \approx 4.384 \mu\text{M}$, and $[R18]_{lb}A_{lb} \approx 6.0 \text{ nM}$. It is desirable to maintain $[R18]_i$ at levels below the CAC value, and this condition is assured by using $[HSA]_0$ in high excess. As $k_{eff} \propto [HSA]_0^{-1}$, increasingly high concentrations of the serum albumin limit the steady-state concentration of monomeric R18 and thus reduce the rate at which the probe is transferred to membranes but not the equilibrium concentration of $[R18]_{lb}$. These results are consistent with the earlier finding of Vaz et al.^{28,29} that serum-bound amphiphiles are not directly exchangeable with membranes. In the present application, a bulk concentration of $[R18]_0 = 4.4 \mu\text{M}$ represents an approximate upper limit concentration of R18 that can be applied to membranes in 0.1% (97 μM) HSA buffer without concern of exceeding the CAC. Therefore, these experimental conditions optimize the kinetics of delivery to bead membranes; k_{eff} is optimized by using a stoichiometric ratio of $[HSA]_0$ and $[R18]_0$ that yields a concentration of monomeric R18 that is just below the aggregation threshold.

Summary and Conclusions

We began this work in order to better understand the process by which R18 distributes between water, serum albumin, and membranes in a model system. We intend to bridge past^{14–17} and current work related to the real-time transfer of R18 from a water/HSA environment into a heterogeneous environment of living cells as outlined in Figure 1. To recapitulate our original goals, in our previous work on cells, we have encountered some difficulty in the quantitative analysis of the transfer of monomeric R18 from the aqueous phase to membranes due to the confounding effects of (a) changes to the spectroscopic characteristics (absorption cross section and emission quantum yield) of R18 due to concentration-dependent aggregation in membranes; a specific problem related with this issue concerns the elucidation of how the spectroscopic changes in the acceptor probes can affect the analysis of FRET data; and (b) probe aggregation at very low concentrations and an undefined critical aggregation constant. To address these issues, we have used monodisperse-sized lipobeads that can support a well-defined number of lipids in a reproducible manner. A titration of increasing mol % R18 into membrane vesicles has enabled the reconstitution of probes whose concentration-dependent quenching is well-defined between 0 and 10 mol %. A novel set of fluorescence calibration beads has proven to be useful in establishing a quantitative basis for analyzing the fluorescence readout of membrane-associated probes by flow cytometry. Addition of exogenous R18 to DOPC and DSC lipobeads has been analyzed according to mass action kinetics in which the transfer of R18 to beads is mediated by serum albumin and defined by phenomenological kinetics. The finding that the site occupancy of exogenous R18 in DOPC and DSC membranes is limited to a few mol % has important implications for FRET in cell membranes. Our analysis of the spectra of R18 monomers and dimers suggest that there is little variation in the spectral overlap integral of either monomeric or dimeric acceptors and FRET donor molecules of interest to our studies (Table 1). We imagine that the limited free-volume capacity of membranes to hold exogenous R18 suggests that differences in κ^2 for mono-

meric and dimeric acceptor conditions are likely to be small at the lower mol % of exogenous R18 due to the notion that probes are expected to be randomly distributed and oriented below a much higher threshold of 10 mol %, at least in L_d phases.^{2,3}

To conclude, this study has examined two limiting models of cell membranes on beads and demonstrated by quantitative measurement the structural differences in L_d DOPC and L_o DSC membranes. In cells, these limiting forms of membrane structure coexist laterally in the plasma membranes. In view of that, the bead assay is conceptually useful in demonstrating, (spectroscopically and quantitatively) how R18 can be used to report the presence of heterogeneous domains. It is then possible to dissect the coexistence of membrane domains in living cells by using FRET to report on the differential kinetics of the localized accumulation of R18 acceptors at two receptor sites, as defined in Figure 1. To recapitulate earlier statements, it is believed that the $\alpha_4\beta_1$ integrin is confined to liquid-disordered domains¹⁷ and that the formyl peptide receptor (FPR) is localized in liquid-ordered domains in the plasma membranes of the same population of U937 cells.²⁶ However, these findings emerged from disparate experimental conditions. Our present study has shown that R18 accumulates differentially in membranes that are modeled after liquid-disordered domains (DOPC) and -ordered domains (DSC). In this regard, we have observed that R18 acceptors differentially accumulate at the sites of $\alpha_4\beta_1$ and FPR expression in living cells (see Supporting Information Figure S1). The model system developed here is applicable to the analysis of these results. A detailed analysis of local FRET at these sites will be published elsewhere.

Acknowledgment. This work was supported by NIH K25AI60036, U54MH074425, HL081062, NSF CTS0332315, and Dedicated Health Research Funds of the University of New Mexico School of Medicine (C-2294-T). Images in this paper were generated in the University of New Mexico Cancer Center Fluorescence Microscopy Facility, supported as detailed on the webpage <http://hsc.unm.edu/crtc/microscopy/Facility.html>. We thank Drs. Ralph Young (Eastman Kodak, Rochester, NY) and Eva Chi (UNM) for stimulating discussions and critical review of our manuscript.

Appendix A. Application of the Steady-State Approximation to the Association of R18 with Lipobeads

From Equation 5

$$\frac{d[R18]}{dt} = -k_1[R18][HSA] + k_{-1}[HSA \cdot R18] - k_2[R18][\text{lipids}] + k_{-2}[R18 \cdot \text{lipids}] = 0 \quad (A1)$$

$$[R18] = \frac{k_{-1}[HSA \cdot R18] + k_{-2}[R18 \cdot \text{lipids}]}{k_1[HSA] + k_2[\text{lipids}]} \quad (A2)$$

substituting A2 into eq 11

$$\frac{d[R18 \cdot \text{lipids}]}{dt} = \left[k_2 \left(\frac{k_{-1}[HSA \cdot R18] + k_{-2}[R18 \cdot \text{lipids}]}{k_1[HSA] + k_2[\text{lipids}]} \right) [\text{lipids}] - k_{-2}[R18 \cdot \text{lipids}] \right] SQ_{[i]} \quad (A3)$$

Because independently measured k_{-2} is small ($1.2 \times 10^{-5} \text{ s}^{-1}$) and $[\text{HSA}]_0 \gg [\text{lipids}]_0$, eq A3 simplifies to

$$\frac{d[\text{R18} \cdot \text{lipids}]}{dt} = \left(\frac{k_2 k_{-1} [\text{HSA} \cdot \text{R18}]}{k_1 [\text{HSA}]} \right) [\text{lipids}] \text{SQ}_{[i]} \quad (\text{A4})$$

Appendix B. Concerning the Equilibrium Distribution of [R18]₀ among Water, Membrane, and Serum Albumin

From eq 5a



at equilibrium

$$[\text{R18} \cdot \text{HSA}]_{\text{eq}} = K_a [\text{R18}]_{\text{eq}} [\text{HSA}]_{\text{eq}} \quad (\text{B2})$$

$$[\text{HSA}]_{\text{eq}} = [\text{HSA}]_0 - [\text{R18} \cdot \text{HSA}] \quad (\text{B3})$$

Substituting eq B2 into B3 and simplifying

$$[\text{R18} \cdot \text{HSA}]_{\text{eq}} = \frac{K_a [\text{R18}]_{\text{eq}} [\text{HSA}]_0}{1 + K_a [\text{R18}]_{\text{eq}}} \quad (\text{B4})$$

The degree of labeling ($[\text{R18}]_{\text{lb}} A_{\text{lb}}$ in eq 14) is governed by a partition coefficient, K_p , which at low concentration of the probe is usually expressed in terms of an equilibrium ratio of the surface concentration of bound probes and free probe in the aqueous phase and has units of length (eq B5).

$$K_p = \frac{[\text{R18}]_{\text{lipobead}} (\text{moles/dm}^2)}{[\text{R18}]_{\text{eq}} (\text{moles/dm}^3)} \quad (\text{B5})$$

$$[\text{R18}]_{\text{eq}} = \frac{[\text{R18}]_{\text{lb}}}{K_p} \quad (\text{B6})$$

then

$$[\text{R18} \cdot \text{HSA}]_{\text{eq}} = \frac{K_a [\text{R18}]_{\text{lb}} [\text{HSA}]_0}{K_p + K_a [\text{R18}]_{\text{lb}}} \quad (\text{B7})$$

At equilibrium, R18 is partitioned according to eq 14 in the text, and substituting the terms in eqs B6 and B7 into eq 14 yields eq B8

$$[\text{R18}]_0 = [\text{R18}]_{\text{lb}} \left(A_{\text{lb}} + \frac{1}{K_p} + \frac{K_a [\text{HSA}]_0}{K_p + K_a [\text{R18}]_{\text{lb}}} \right) \quad (\text{B8})$$

References and Notes

- (1) Yamazaki, I.; Tamai, N.; Yamazaki, T. *J. Phys. Chem.* **1990**, *94*, 516–525.
- (2) Ediger, M. D.; Domingue, R. P.; Fayer, M. D. *J. Chem. Phys.* **1984**, *80*, 1246–1253.
- (3) Baumann, J.; Fayer, M. D. *J. Chem. Phys.* **1986**, *1*, 4087–4107.
- (4) Nakashima, K.; Duhamel, J.; Winnik, M. A. *J. Phys. Chem.* **1993**, *14*, 10702–10707.
- (5) Leenhouts, J. M.; Dekruiff, B. *Biochim. Biophys. Acta* **1995**, *26*, 121–126.
- (6) Wunderliallenspach, H.; Gunthert, M.; Ott, S. *Biochemistry* **1993**, *26*, 900–907.
- (7) Stegmann, T.; Schoen, P.; Bron, R.; Wey, J.; Bartoldus, I.; Ortiz, A.; Nieva, J. L.; Wilschut, J. *Biochemistry* **1993**, *26*, 11330–11337.
- (8) Macdonald, R. I. *J. Biol. Chem.* **1990**, *15*, 13533–13539.
- (9) Pozzi, D.; Lisi, A.; Deros, I.; Ferroni, L.; Giuliani, A.; Ravagnan, G.; Grimaldi, S. *Photochem. Photobiol.* **1993**, *57*, 426–430.
- (10) Melikyan, G. B.; Deriy, B. N.; Ok, D. C.; Cohen, F. S. *Biophys. J.* **1996**, *71*, 2680–91.
- (11) Niles, W. D.; Cohen, F. S. *J. Gen. Physiol.* **1991**, *97*, 1101–1119.
- (12) Hoekstra, D.; Deboer, T.; Klappe, K.; Wilschut, J. *Biochemistry* **1984**, *23*, 5675–5681.
- (13) Stegmann, T.; Hoekstra, D.; Scherphof, G.; Wilschut, J. *J. Biol. Chem.* **1986**, *25*, 10966–10969.
- (14) Chigaev, A.; Waller, A.; Zwart, G. J.; Buranda, T.; Sklar, L. A. *J. Immunol.* **2007**, *178*, 6828–6839.
- (15) Larson, R. S.; Davis, T.; Bologa, C.; Semenuk, G.; Vijayan, S.; Li, Y.; Oprea, T.; Chigaev, A.; Buranda, T.; Wagner, C. R.; Sklar, L. A. *Biochemistry* **2005**, *44*, 4322–4331.
- (16) Chigaev, A.; Zwart, G. J.; Buranda, T.; Edwards, B. S.; Prossnitz, E. R.; Sklar, L. A. *J. Biol. Chem.* **2004**, *279*, 32435–32443.
- (17) Chigaev, A.; Buranda, T.; Dwyer, D. C.; Prossnitz, E. R.; Sklar, L. A. *Biophys. J.* **2003**, *85*, 3951–3962.
- (18) Mutucumarana, V. P.; Duffy, E. J.; Lollar, P.; Johnson, A. E. *J. Biol. Chem.* **1992**, *267*, 17012–17021.
- (19) Yegneswaran, S.; Smirnov, M. D.; Safa, O.; Esmon, N. L.; Esmon, C. T.; Johnson, A. E. *J. Biol. Chem.* **1999**, *274*, 5462–5468.
- (20) Yegneswaran, S.; Wood, G. M.; Esmon, C. T.; Johnson, A. E. *J. Biol. Chem.* **1997**, *272*, 25013–25021.
- (21) Wolber, P. K.; Hudson, B. S. *Biophys. J.* **1979**, *28*, 197–210.
- (22) Jacobson, K.; Mouritsen, O. G.; Anderson, R. G. *Nat. Cell Biol.* **2007**, *9*, 7–14.
- (23) Anderson, R. G.; Jacobson, K. *Science* **2002**, *296*, 1821–1825.
- (24) Edidin, M. *Annu. Rev. Biophys. Biomol. Struct.* **2003**, *32*, 257–283.
- (25) Simons, K.; Vaz, W. L. C. *Annu. Rev. Biophys. Biomol. Struct.* **2004**, *33*, 269–295.
- (26) Xue, M.; Vines, C. M.; Buranda, T.; Cimino, D. F.; Bennett, T. A.; Prossnitz, E. R. *J. Biol. Chem.* **2004**, *279*, 45175–45184.
- (27) Nakashima, K.; Fujimoto, Y. *Photochem. Photobiol.* **1994**, *60*, 563–566.
- (28) Abreu, M. S. C.; Estronca, L.; Moreno, M. J.; Vaz, W. L. C. *Biophys. J.* **2003**, *84*, 386–399.
- (29) Estronca, L.; Moreno, M. J.; Laranjinha, J. A. N.; Almeida, L. M.; Vaz, W. L. C. *Biophys. J.* **2005**, *88*, 557–565.
- (30) Selwyn, J. E.; Steinfeld, J. I. *J. Phys. Chem.* **1972**, *76*, 762–774.
- (31) McConnell, H. M.; Radhakrishnan, A. *Biochim. Biophys. Acta* **2003**, *10*, 159–173.
- (32) Radhakrishnan, A.; McConnell, H. *Proc. Natl. Acad. Sci. U.S.A.* **2005**, *102*, 12662–12666.
- (33) Demel, R. A.; Vandeene, L. L.; Bruckdor, K. R. *Biochim. Biophys. Acta* **1972**, *255*, 311.
- (34) Dietrich, C.; Bagatolli, L. A.; Volovyk, Z. N.; Thompson, N. L.; Levi, M.; Jacobson, K.; Gratton, E. *Biophys. J.* **2001**, *80*, 1417–1428.
- (35) Buranda, T.; Huang, J.; Rama Rao, G. V.; Ista, L. K.; Larson, R. S.; Ward, T. L.; Sklar, L. A.; Lopez, G. P. *Langmuir* **2003**, *19*, 1654–1663.
- (36) Wu, Y.; Campos, S. K.; Lopez, G. P.; Ozbun, M. A.; Sklar, L. A.; Buranda, T. *Anal. Biochem.* **2007**, *364*, 180–192.
- (37) Wu, Y.; Lopez, G. P.; Sklar, L. A.; Buranda, T. *Anal. Biochem.* **2007**, *364*, 193–203.
- (38) Stottrup, B. L.; Stevens, D. S.; Keller, S. L. *Biophys. J.* **2005**, *88*, 269–76.
- (39) Parker, C. A. *Photoluminescence of Solutions*; Elsevier: Amsterdam, The Netherlands, 1968.
- (40) Bhattacharya, A. A.; Grune, T.; Curry, S. *J. Mol. Biol.* **2000**, *10*, 721–732.
- (41) Sklar, L. A.; Hudson, B. S.; Simoni, R. D. *Biochemistry* **1977**, *16*, 5100–5108.
- (42) Demant, E. J.; Richieri, G. V.; Kleinfeld, A. M. *Biochem. J.* **2002**, *363*, 809–815.
- (43) Spector, A. A. *J. Lipid Res.* **1975**, *16*, 165–179.
- (44) Pownall, H. J. *J. Mol. Neurosci.* **2001**, *16*, 2–3.
- (45) Zakim, D. *J. Membr. Biol.* **2000**, *15*, 101–109.

Supporting Information Available: Figure S1. This material is available free of charge via the Internet at <http://pubs.acs.org>.

- (46) Kleinfeld, A. M. *J. Membr. Biol.* **2000**, *15*, 79–86.
- (47) Vaz, W. L. C.; Melo, E. *J. Fluoresc.* **2001**, *11*, 255–271.
- (48) Tanford, C. *The Hydrophobic Effect: Formation of Micelles and Biological Membranes*; Wiley-InterScience: New York, 1980.
- (49) Almeida, P. F. F.; Vaz, W. L. C.; Thompson, T. E. *Biochemistry* **1992**, *31*, 6739–6747.
- (50) Marrink, S. J.; Sok, R. M.; Berendsen, H. J. C. *J. Chem. Phys.* **1996**, *104*, 9090–9099.
- (51) Gennis, R. B. *Biomembranes — Molecular Structure and Functions*; Springer-Verlag: New York, 1989.
- (52) Ramette, R. W.; Sandell, E. B. *J. Am. Chem. Soc.* **1956**, *78*, 4872–4878.
- (53) McRae, E. G.; Kasha, M. *J. Chem. Phys.* **1961**, *11*, 38.
- (54) Valdes-Aguilera, O.; Neckers, D. C. *Acc. Chem. Res.* **1989**, *22*, 171–177.
- (55) Rohatgi, K. K.; Singal, G. S. *J. Phys. Chem.* **1966**, *70*, 1695–1701.
- (56) Drexhage, In *Dye Lasers*; Schafer, F., Ed.; Springer-Verlag: Heidelberg, Germany, 1989; Vol. 1, pp 155–189.
- (57) Kasha, M. *Radiat. Res.* **1963**, *20*, 55–71.
- (58) Johansson, L. B. A.; Niemi, A. *J. Phys. Chem.* **1987**, *21*, 3020–3023.
- (59) Cerione, R. A.; McCarty, R. E.; Hammes, G. G. *Biochemistry* **1983**, *22*, 769–776.
- (60) Birks, J. B. *Photophysics of Aromatic Molecules*; Wiley-InterScience: New York, 1970.
- (61) Mukerjee, P. *J. Phys. Chem.* **1965**, *69*, 2821–2827.
- (62) Lakowicz, J. R. *Principles of Fluorescence Spectroscopy*, 2 ed.; Plenum Press: New York, 1999.
- (63) Dale, R.; Eisinger, J.; Blumberg, W. *Biophys. J.* **1979**, *26*, 161–194.
- (64) Dale, R. E. Orientational Averaging in Long-Range Excitation Energy Transfer Ensembles of Various Dimensionalities; In *Conference Digest*, 3rd Conference on Luminescence, Szeged, Hungary, 1979; Vol. 2.
- (65) Baksh, M. M.; Jaros, M.; Groves, J. T. *Nature* **2004**, *427*, 139–41.
- (66) Boxer, S. G. *Current Opin. Chem. Biol.* **2000**, *4*, 704–709.
- (67) Sackmann, E. *Science* **1996**, *271*, 43–48.
- (68) Salafsky, J.; Groves, J. T.; Boxer, S. G. *Biochemistry* **1996**, *35*, 14773–14781.
- (69) Veatch, S. L.; Keller, S. L. *Phys. Rev. Lett.* **2005**, *94*, 148101.
- (70) Nolan, J. P.; Sklar, L. A. *Nat. Biotechnol.* **1998**, *16*, 633–638.
- (71) Nichols, J. W.; Pagano, R. E. *Biochemistry* **1982**, *21*, 1720–1726.
- (72) Sampaio, J. L.; Moreno, M. J.; Vaz, W. L. *Biophys. J.* **2005**, *88*, 4064–4071.
- (73) Abreu, M. S.; Moreno, M. J.; Vaz, W. L. *Biophys. J.* **2004**, *87*, 353–365.
- (74) Nichols, J. W.; Pagano, R. E. *J. Biol. Chem.* **1983**, *258*, 5368–5371.
- (75) Nichols, J. W. *Biochemistry* **1985**, *24*, 6390–6398.
- (76) Richieri, G. V.; Ogata, R. T.; Kleinfeld, A. M. *J. Biol. Chem.* **1996**, *10*, 11291–11300.
- (77) Wu, Y.; Zwartz, G.; Lopez, G. P.; Sklar, L. A.; Buranda, T. *Cytometry A* **2005**, *67*, 37–44.
- (78) Benson, S. W. *Foundations of Chemical Kinetics*; McGraw-Hill: New York, 1960.
- (79) Motulsky, H. J.; Mahan, L. C. *Mol. Pharmacol.* **1984**, *25*, 1–9.
- (80) Aniansson, E. A. G.; Wall, S. N.; Almgren, M.; Hoffmann, H.; Kielmann, I.; Ulbricht, W.; Zana, R.; Lang, J.; Tondre, C. *J. Phys. Chem.* **1976**, *80*, 905–922.
- (81) Nagarajan, R.; Ruckenstein, E. *Langmuir* **1991**, *7*, 2934–2969.
- (82) Maher, P.; Singer, S. J. *Biochemistry* **1984**, *23*, 232–40.
- (83) Abreu, M. S. C.; Moreno, M. J.; Vaz, W. L. C. *Biophys. J.* **2004**, *87*, 353–365.
- (84) Dietrich, C.; Volovyk, Z. N.; Levi, M.; Thompson, N. L.; Jacobson, K. *Proc. Natl. Acad. Sci. U.S.A.* **2001**, *11*, 10642–10647.
- (85) Falck, E.; Patra, M.; Karttunen, M.; Hyvonen, M. T.; Vattulainen, I. *Biophys. J.* **2005**, *89*, 745–752.
- (86) Falck, E.; Patra, M.; Karttunen, M.; Hyvonen, M. T.; Vattulainen, I. *Biophys. J.* **2004**, *87*, 1076–1091.
- (87) Burns, A. R.; Frankel, D. J.; Buranda, T. *Biophys. J.* **2005**, *89*, 1081–1093.
- (88) Almeida, P. F.; Vaz, W. L.; Thompson, T. E. *Biophys. J.* **2005**, *88*, 4434–4438.
- (89) Massari, S.; Colonna, R.; Folena, E. *Biochim. Biophys. Acta* **1988**, *9*, 149–157.

JP906648Q